Supplementary information for

Mapping strong electronic coupling in metavalent PbS moiré superlattices

Yu Wang[1,2,†], Zhigang Song[1,†], Jiawei Wan[1,2], Sophia Betzler[1], Yujun Xie[1], Colin Ophus[3], Karen C. Bustillo[3], Peter Ercius[3], Lin-Wang Wang[1], and Haimei Zheng[1,2,*]

Affiliations:

[1]Materials Sciences Division, Lawrence Berkeley National Laboratory, Berkeley, CA 94720, USA.

[2]Department of Materials Science and Engineering, University of California, Berkeley, Berkeley, CA 94720, USA.

[3]National Center for Electron Microscopy, Molecular Foundry, Lawrence Berkeley National Laboratory, Berkeley, CA 94720, USA.

[†]Contributed equally to this work.

[*]To whom correspondence should be addressed; E-mail: hmzheng@lbl.gov

This PDF file includes:

1 Geometry of PbS moiré superlattices

In the main text, we describe two calculation approaches for evaluating the structural and electronic properties of PbS moiré superlattices: 1. constructing small unit cells with laterally shifted bilayer nanosheets, and 2. directly calculating large moiré unit cells with commensurate angles. In this section, we further discuss the geometry of PbS moiré superlattices and elaborate why and how we construct the structures for two calculation approaches.

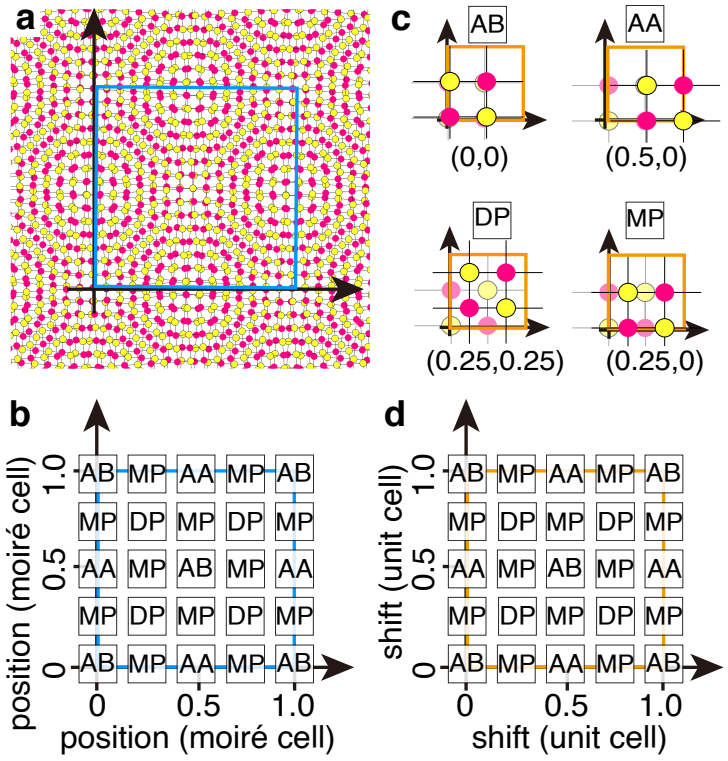

Fig. S1 | Approximation of moiré superlattices through laterally shifted small cells. **a**, Illustration of a small-angle twisted moiré superlattice. The blue square indicates the periodic moiré cell. **b**, Representative stacking configurations marked inside the periodic moiré cell. **c**, Representative stacking configurations obtained by shifting the upper layer nanosheet with different values. The orange square indicates the periodic unit cell of non-twisted bilayer nanosheets. **d**, Periodic stacking configurations obtained by shifting the upper layer nanosheet with different values. Labels represent shift vectors within one unit cell and their corresponding stacking configurations.

Fig. S1a,b show the local stacking configurations and their periodic arrangement in a small-angle twisted moiré superlattice. When the twist angle is close to zero, the local stacking configurations can be approximated to laterally shifted bilayer nanosheets. Fig. S1c shows that representative configurations (i.e., AB, AA, MP, and DP) are constructed through laterally shifting the upper layer of bilayer nanosheets in a small unit cell with specific shifting vectors. The correspondence between the stacking configurations and the shifting vectors is demonstrated in

Fig. S1d, matching the pattern of stacking configurations in Fig. S1b. Therefore, we can use the laterally shifted small cells to approximately evaluate the stacking configurations in a moiré superlattice when the twist angle is small.

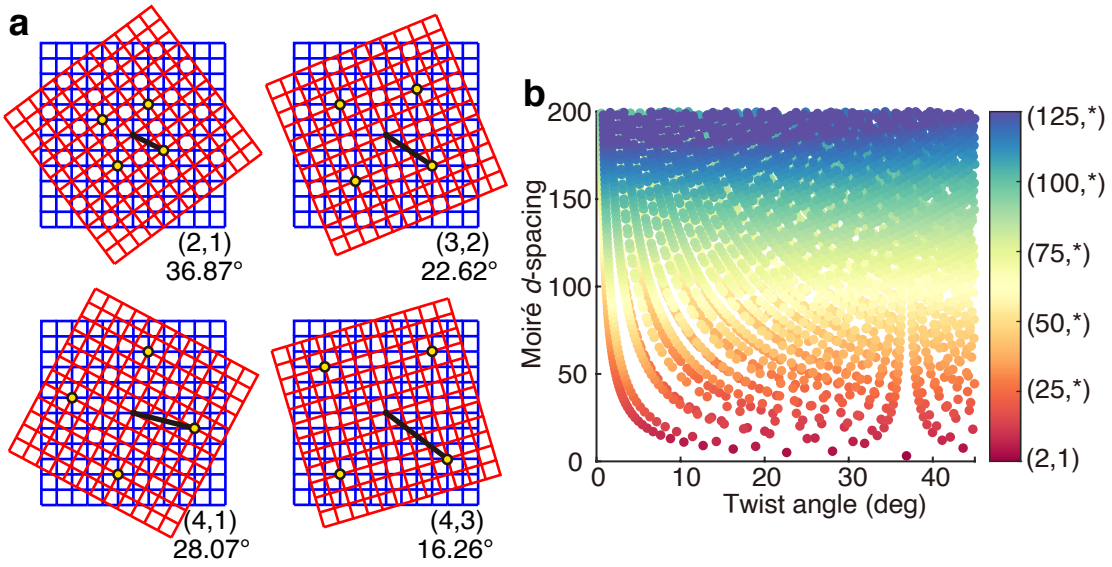

Fig. S2 | Construction of commensurate moiré superlattices. **a**, Representative periodic moiré supercells obtained by twisting two atomic lattices with commensurate angles. Red and blue grids represent the upper and lower atomic lattices, respectively. Yellow dots mark the four corners of the formed moiré supercells. The yellow dot linked by the black line originally locates at (m,n) in the red grid coordinate and turns to $(m,-n)$ in the blue grid coordinate after a clockwise twisting. (m,n) values and the twist angles are labelled beneath the grids. **b**, Moiré d-spacing as a discrete function of twist angle. The colourmap is created based on the m value in (m,n).

Direct calculations are based on the construction of moiré superlattices with commensurate angles. 2D PbS nanocrystals have a square lattice and can be simplified as grids as in Fig. S2a. When the upper grid (red) turns clockwisely, a specific dot marked as (m,n) can overlap with the $(m,-n)$ dot in the lower grid (blue), thus forming superlattices with commensurate angles. The values of (m,n) leading to unique moiré superlattices are derived through mathematical analysis based on the following two rules: 1. m and n must be one odd and one even, 2. m and n cannot have a common divisor greater than one. The first four examples are shown in Fig. S2a, and the relationship between moiré d-spacing and the twisted angles are shown in Fig. S2b. The largest moiré cell we directly calculated in this work is built on the (m,n) value of (33,1), which has a twist angle of 3.47° and contains 4360 atoms.

2 Synthetic mechanism of PbS nanosheets

We investigate the synthetic mechanism of PbS nanosheets by stopping the reaction earlier at 12 min (20 min for the standard procedure) and washing the product only twice with water. We observe the coexistence of PbS nanoparticles and nanosheets in the intermediate product as shown in Fig. S3. The size distribution of nanoparticles is determined by image recognition and statistical analysis. Most nanoparticles have a diameter around 3 nm, approximate to the thickness of individual nanosheet (characterized in Fig. 2). Therefore, we conjecture that the aqueous synthesis of PbS nanosheets may undergo an oriented attachment process from nanoparticles to nanosheets. A similar oriented attachment route has been proposed for the synthesis of PbS nanosheets in organic solvents[1].

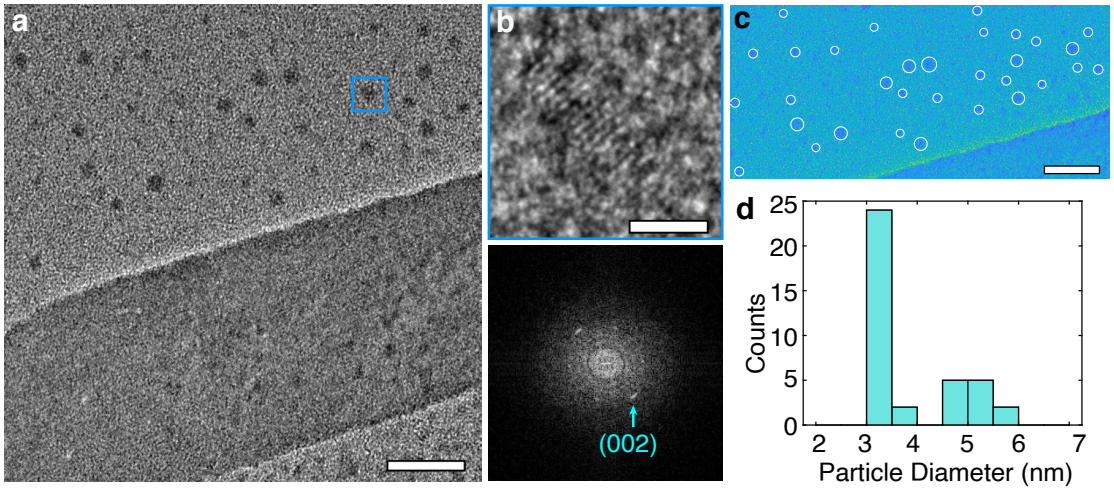

Fig. S3 | Nanoparticles observed during synthesis. **a**, TEM image of nanoparticles scattered around a PbS nanosheet. The sample was prepared with the standard synthesis procedure of PbS nanosheets and only washed twice with water. **b**, Enlarged image (upper) and the FFT image (lower) of the boxed nanoparticle in panel a. Diffraction dots match the (002) d-spacing of PbS rock-salt structure. **c**, Recognition of the contour of nanoparticles for statistically analysing their size. **d**, Histogram of the size of observed nanoparticles. Scale bars: 20 nm in a and c, 2 nm in b.

3 Self-rolling behaviour of discrete nanosheets

We find that some discrete nanosheets undergo a self-rolling process after ligand removal, especially when the samples are left in liquid phase for a longer time (i.e., 12 hours). Fig. **S4** shows two nanosheets self-rolled to two different extents. The nanosheet in Fig. **S4**a has its bottom part partially rolled, whereas the top part remains mainly flat. The nanosheet in Fig. **S4**b has its right half fully rolled. These rolled structures provide an alternative route for measuring the thickness of nanosheets, giving consistent results (approximately 3 nm) to the side-view measurement in Fig. 2. This self-rolling behaviour shows the considerable deformability of naked ultra-thin PbS nanosheets. The driving force for self-assembling into moiré superlattices and the driving force for self-rolling are probably the same, i.e., for reducing the surface energy. We found the self-rolling behaviour in discrete nanosheets, but not in moiré superlattices, suggesting that forming superlattices is an effective way to stabilize the naked nanosheets.

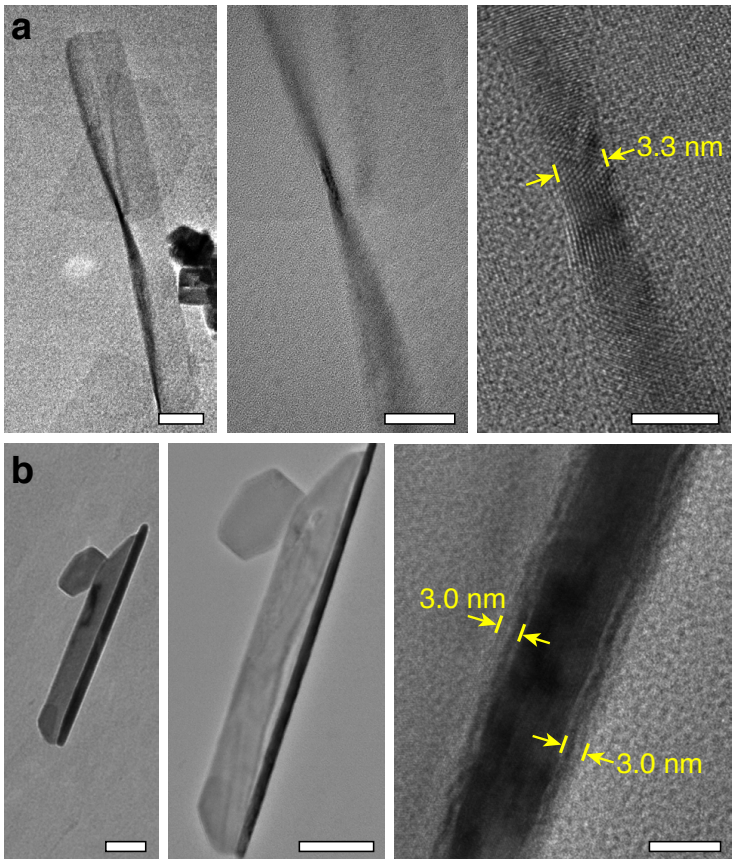

Fig. S4 | Self-rolling behaviour of individual PbS nanosheets. **a**, TEM images with different magnifications of a nanosheet with the bottom part partially rolled. **b**, TEM images with different magnifications of a nanosheet with the right half rolled. Scale bars: a, 50, 20, and 5 nm (left to right); b, 100, 100, and 10 nm (left to right).

4 Simulation of side-view images

The lattice spacings in the superlattice are measured in real space based on the comparison of experimental and simulated side-view TEM images, as shown in Fig. S5. The structure used for TEM image simulations is built based on the DFT calculated moiré superlattice with a 6.06° twist angle. The TEM images were simulated through a multislice code, compuTEM[2], with partial coherence (300 keV, Cs = 0.01 mm, 0.5 mrad convergence). We performed the simulation with a variety of defocus (from -12 to 12 nm) and thickness (from 20 to 50 nm). The different thickness has trivial impact on the simulated images, whereas the different defocus changes the result dramatically (Fig. S5). For example, in the underfocused case (Fig. S5a), the lattice spacings should be measured by the distance between the white stripes or dots; whereas in the overfocused case (Fig. S5c), they should be measured by the distance between the black stripes or dots. But in all cases, the measurement of lattice spacings can distinguish the difference between the interfacial distance (marked by black arrows) and the interlayer distances inside a nanosheet (marked by magenta or orange arrows). Overall, the experimental image is closer to the underfocused image (Fig. S5a). Therefore we measured the lattice spacing by finding the the local maxima (white dots or strips) of the experimental images, as shown in Fig. 2i.

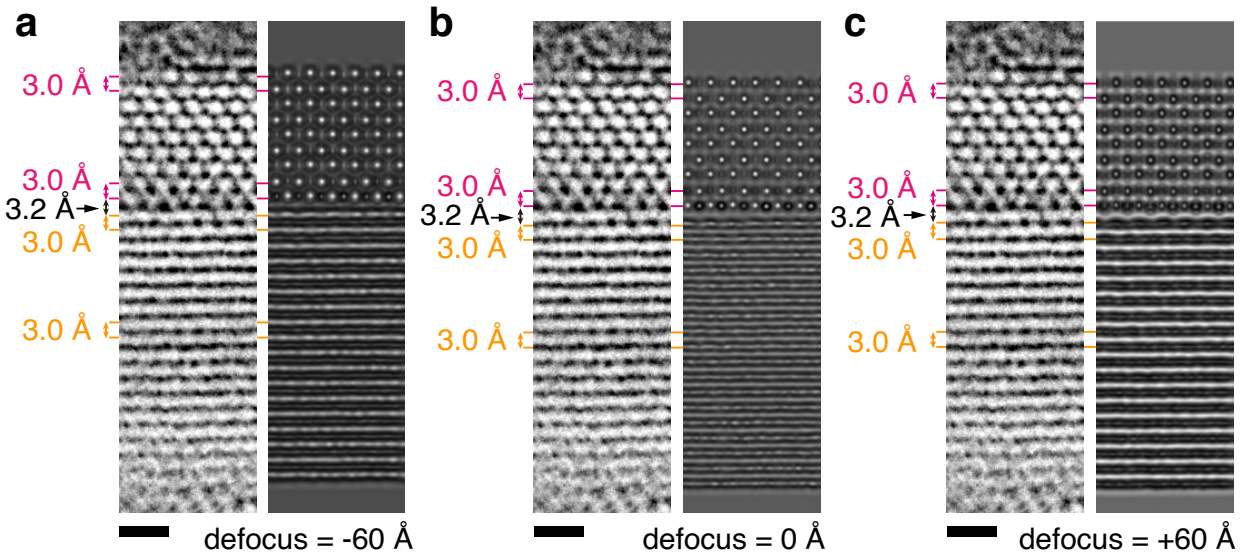

Fig. S5 | Comparison of experimental and simulated side-view images. **a**–**c**, Left are the same experimental side-view image, extracted from the boxed area of Fig. 2h. Right are the simulated images with different defocus values of -60, 0, and 60 Å, respectively. Magenta and orange lines mark the representative atomic layers inside nanosheet L1 and L2, respectively. Black arrows marks the interfacial distance between L1 and L2. All scale bars are 1 nm.

5 Localized electron excitation in small-angle twisted moiré superlattices

In Fig. 3 and Extended Data Fig. 6, we used a qualitative blue–red–yellow colormap to visualize the EELS mapping, showing the localization of electron excitation in the moiré superlattice with a twist angle of 1.3°. Here we present the additional visualization of the EELS mapping with two continuous colormaps, i.e., viridis and blue–white–red–yellow, in Fig. **S6**. The visualization with all colormaps leads to the same conclusion that the segregated pattern in the double-layer region only appear at the smallest twist angle of 1.3°, not at the 3.0° and 4.6°. Because the three moiré superlattices in Fig. **S6**a were imaged in one experiment with identical conditions, we can compare the thickness of individual nanosheets from their intensities in the STEM images. We find that all individual nanosheets in the three moiré superlattices have a similar thickness with less than 10% difference. Moreover, even the thickness difference of nanosheets could alter the EELS absorption, its modulation would be uniform if not considering the effect of moiré patterns. Therefore, the distinctive lower-energy spectra with the peak lower than 1.68 eV (corresponding to the blue regions) of the 1.3° twisted superlattices are resulted from the effect of twist angle instead of the thickness difference.

The segregation pattern of the 1.3° twisted superlattices generally matches the simulated pattern of AA, AB, and DP configurations in the visualizations with all colormaps. The qualitative difference between the experimental and the simulated patterns may arise from current experimental limitation of EELS and/or structural deformation. Although we employ state-of-art Continuum Gatan Imaging Filter (GIF) spectrometer, the signal-to-noise ratio of individual low-loss spectrum at 1–2 eV is still low, especially when we are trying to push for high spatial resolution. In addition, during the EELS measurement, moiré superlattices are suspended over vacuum without mechanical support of a substrate. Given the deformability of ultrathin PbS nanosheets, it is possible that the superlattices could move (perpendicular to the electron beam) or slightly bend (along the electron beam) during the EELS acquisition that usually takes minutes. Despite of the qualitative difference, the overall shape and the size/distance of each region in the experimental pattern match the simulated pattern well.

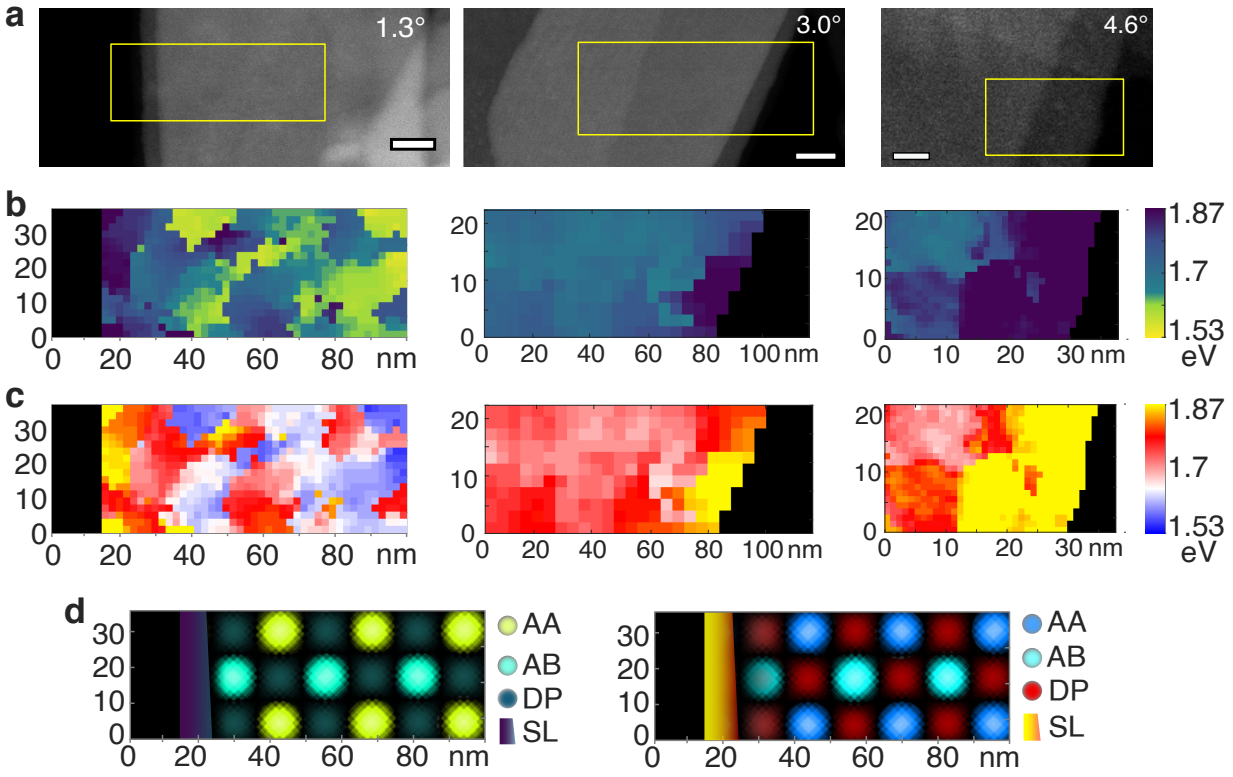

Fig. S6 | EELS mapping visualized with different colormaps. **a**, Survey image of three moiré superlattices. Yellow box marks the scanning region for STEM-EELS. Three columns in a–c correspond to the twist angles of 1.3°, 3.0°, and 4.6°, respectively. Scale bar: 20, 20, and 10 nm (left to right). **b**,**c**, 2D mapping of the energy of absorption peaks with a viridis (b) or a blue–white–red–yellow (c) colormap. In both cases, the colormap is consistent for three superlattices with colorbar labelled beside the right column. **d**, Simulated pattern of AA, AB, and DP configurations and single layer (SL) in the 1.3° twisted superlattice with viridis (left) or a blue–white–red–yellow (right) colormap.

6 Calculation of the valleytronic properties

Valleytronics has been widely investigated in hexagonal two-dimension materials such as MoS_2 and graphene[3]. According to our DFT calculations, some PbS moiré superlattices also have valley degree of freedom. PbS moiré superlattices not only provide stronger interlayer coupling over these conventional vdW materials, but only exhibits a different square symmetry, leading to a significant difference in valleytronics.

Fig. S7 shows the calculated valleytronic property of two PbS superlattices with 0 and 36.87°. Both structures have direct bandgap, and the band edges are localized at four different momentum positions in the reciprocal space. Because valleys with opposite momentum are equal, these four valleys can be divided into two pairs, forming valley pseudo-spins. Different valley pairs should response differently to external fields, such as mechanic strain and photons[4]. Here, we also calculate the response of two superlattices upon polarized photons, and the linear polarization of optical transition is shown in the middle paddles of Fig. S7. The linear polarization is defined as:

$$\eta(\mathbf{k}) = \frac{|\langle\psi_v(\mathbf{k})|P_x|\psi_c(\mathbf{k})\rangle|^2 - |\langle\psi_v(\mathbf{k})|P_y|\psi_c(\mathbf{k})\rangle|^2}{|\langle\psi_v(\mathbf{k})|P_x|\psi_c(\mathbf{k})\rangle|^2 + |\langle\psi_v(\mathbf{k})|P_y|\psi_c(\mathbf{k})\rangle|^2} \tag{1}$$

where P_x and P_y are normal momentum projection in the x- and y-direction, and the $\psi_c(\mathbf{k})$ and $\psi_v(\mathbf{k})$ are wave functions of the conduction and valence bands, respectively.

As shown by the middle paddles in Fig. S7, the different twisting of PbS superlattices leads to a significant difference on the response to the polarized photons, demonstrating the valley controllability by forming moiré superlattices. Moreover, the linear polarization exhibits the same amplitude but opposite sign for different valley pairs. This indicates the opposite polarization of the absorbed and emitted photons for different valley pairs, which provides the potential for

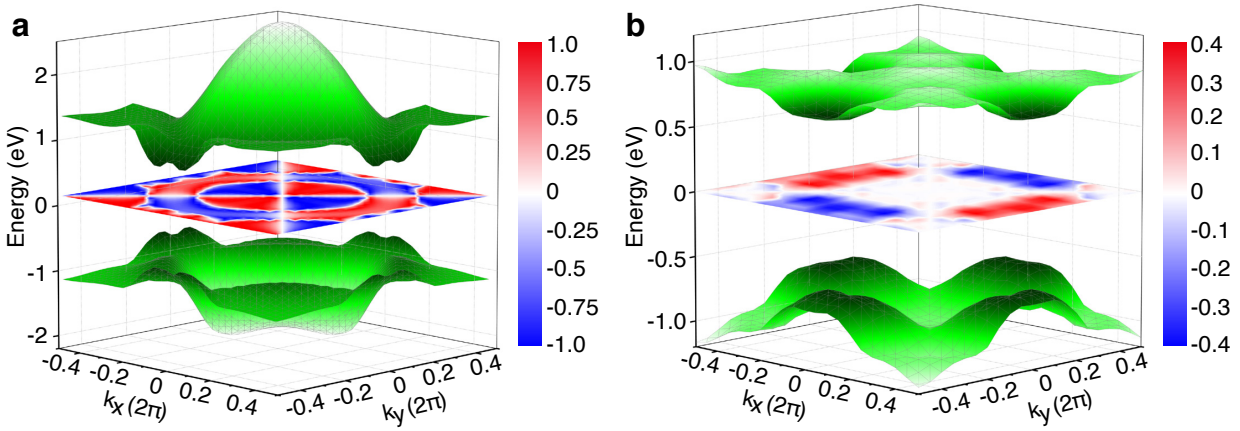

Fig. S7 | Calculated valleytronic properties. Valence band (top surface), conduction band (bottom surface), and degree of linear polarization (middle image) of two bilayer superlattices. **a**, Non-twisted bilayer. **b**, Moiré superlattice with a twist angle of 36.87°.

designing polarized photoelectric devices[5]. For example, different valley pairs can be controlled by pumping one of the valley pairs by a polarized laser, which creates non-equal carriers at different valley pairs despite of their degenerated energy levels. Materials possessing non-equal valleys are rare. Metavalent moiré superlattices provides opportunities to synthesize valleytronic materials and great valley controllability.

References

[1] Schliehe, C. *et al.* Ultrathin PbS sheets by two-dimensional oriented attachment. *Science* **329**, 550–553 (2010).

[2] Kirkland, E. J. *Advanced computing in electron microscopy* (Springer, 1998).

[3] Schaibley, J. R. *et al.* Valleytronics in 2D materials. *Nat. Rev. Mater.* **1**, 1–15 (2016).

[4] Wan, W., Yao, Y., Sun, L., Liu, C.-C. & Zhang, F. Topological, valleytronic, and optical properties of monolayer PbS. *Adv. Mater.* **29**, 1604788 (2017).

[5] Song, Z. *et al.* Spontaneous valley splitting and valley pseudospin field effect transistors of monolayer $VAgP_2Se_6$. *Nanoscale* **10**, 13986–13993 (2018).